Research Article | Vol. 29, No. 20 / 27 Sep 2021 / Optics Express 31212
Optics EXPRESS

Design of reconfigurable on-chip wireless interconnections through Optical Phased Arrays

GIOVANNA CALÒ,[1,*] GAETANO BELLANCA,[2] MARINA BARBIROLI,[3] FRANCO FUSCHINI,[3] GIOVANNI SERAFINO,[4] DAVIDE BERTOZZI,[2] VELIO TRALLI,[2] AND VINCENZO PETRUZZELLI[1]

[1]*Department of Electrical and Information Engineering, Polytechnic University of Bari, Via Orabona, 4, Bari 70125, Italy*
[2]*Department of Engineering, University of Ferrara, Via Saragat, 1, Ferrara 44122, Italy*
[3]*Department of Electrical, Electronic and Information Engineering "G. Marconi", University of Bologna, Viale del Risorgimento, 2, Bologna 40136, Italy*
[4]*Scuola Superiore Sant'Anna, TeCIP Institute, via G. Moruzzi 1, 56124 Pisa, Italy*
[*]*giovanna.calo@poliba.it*

Abstract: In this paper we report the design of a device allowing on-chip optical wireless interconnections, based on transmitting and receiving Optical Phased Arrays (OPA). The proposed device aims at realizing high-bandwidth and power-efficient reconfigurable connections between multiple nodes, e.g. chiplets stacked onto a common silicon interposer in 2.5D manycore systems. The communication through an optical wireless switch is a completely novel approach to overcome the bottleneck of wired communication and to provide flexibility in the network topology configuration. We report the OPA design criteria as well as the results of three-dimensional Finite Difference Time Domain (FDTD) simulations. We exploit the in-plane radiation of simple taper antennas to implement 1×N and N × N switching matrices. The effect of the multipath propagation in the on-chip multi-layered medium is also taken into account.

1. Introduction

Computing architectures at all scales are striving to keep up with the high-performance requirements of data-oriented analytics, while meeting constant power and thermal budgets [1]. As a result, new solutions for dense system-level integration are gaining momentum, such as 3D stacking or 2.5D integration. These solutions call for Tb/s-scale bandwidth densities and communication power efficiencies, that are out-of-reach for conventional electronics [2].

Chip-scale connectivity has been traditionally delivered through Networks-on-Chip (NoCs), where different cores are connected through electrical links and switching fabrics [3]. However, emerging data-intensive applications are bringing fundamental scalability bottlenecks to the forefront [4], especially its latency-inefficient multi-hop nature and a growing gap in the delivered communication bandwidth. The need of new solutions for interconnect technologies is clear and well-known [5].

A paradigm shift was achieved by the onset of Optical Networks-on-Chip (ONoC), enabled by the relentless penetration of photonic technology into smaller and smaller-scale systems traditionally dominated by electronics [6]. Especially in datacenters, ONoCs are being assessed for rack- and board-scale optical interconnection architectures, and claim massive any-to-any, buffer-less, collision-less and extremely low-latency switching platforms with bandwidth densities in the order of tens of Tb/s [7], which pave the way for their future deployment also at the chip scale to support 3D [8] or 2.5D integration [9].

The most common implementation for ONoCs is based on "wired" (i.e. waveguide-based) optical connections and routing matrices that exploit the resonant behavior of micro-ring resonators (MRR) [10–13]. The resonant nature of MRRs represents per se a possible bandwidth limitation

#427633 https://doi.org/10.1364/OE.427633
Journal © 2021 Received 14 Apr 2021; revised 12 Jun 2021; accepted 24 Jun 2021; published 14 Sep 2021

Optics EXPRESS

when Tb/s rates must be attained, unless cascades of a large number of rings are employed. As a fact, as the network size scales up and the number of transmitters and receivers increases, the power efficiency and communication reliability claims of ONoCs become progressively impaired [12]. The increase of insertion losses along optical paths, the proliferation of MRR devices, the need to fine-tune the resonant wavelengths through thermal tuning, and the number of wavelength-division multiplexed channels to support bandwidth density overall result in expensive static power budgets. The current trend in ONoCs is thus the definition of network topologies that minimize the overall number of resonant devices and that try to reduce the topological complexity [14].

Wireless on-chip networks (WiNoCs) have also been proposed as an alternative paradigm for the communication between different chips and, in most advanced proposals, between different cores [15–17]. The possibility of removing the overhead of network topology is indeed a great advantage of wireless communication. However, unless very high frequencies are chosen, such networks are limited by the size of the antennas and, consequently, by the chip area usage. Radio Frequency (RF) communication, which is the most mature wireless technology to date, results in bulky solutions which are impractical for NoC integration. The mm-wave or THz ranges indeed appear to be more suitable for on-chip integration, thanks to the smaller sizes of the antennas and to the achievable data rates of tens of Gb/s. For example, line-of-sight (LoS) links have been experimentally demonstrated at 142 GHz achieving data rates of 14 Gb/s over distances of 0.6 mm through silicon integrated antennas [18]. For on chip communication, graphene-based THz antennas are one of the most promising technologies, since the size of the radiators can be reduced up to a few tens of microns thanks to the occurrence of plasmonic resonance [19]. However, the on-chip integration of such antennas and of THz transceivers still requires intensive research and, to the best of our knowledge, is not yet mature.

In this picture, optical wireless technology can provide attractive interconnect solutions, offering advantages in terms of data format and throughput transparency, and low sensitivity to inter-device electro-magnetic interference. Furthermore, the recent impressive advances in photonic integrated technologies allow for a reduction in footprint and power consumption, making photonics systems deployable at a chip-level scale. Among the photonic integration platforms, Silicon photonics [20] is particularly attractive. One reason is the high index contrast which, entailing a strong field confinement, allows for low propagation losses and waveguides with small bending radii. Moreover, thanks to its compatibility with CMOS processes [21], grants the possibility of exploiting CMOS fabrication facilities and integrating electronic and photonic devices on the same chip. Optical wireless interconnect technology has been recently proposed to exploit the best of both wireless and optical communications [22,23]. Different antennas have been investigated for on-chip wireless communication based on dielectric or plasmonic radiators [24–27]. Point-to-point links have been numerically and experimentally demonstrated [22,23] as well as beam steering through antenna arrays [22,25]. In particular, a 1×N reconfigurable wireless switch, enabling beam steering of the transmitted signal by the phase shifting of an input antenna array, was reported in [22]. In this case, the transmitted signal is received by N single antennas (i.e. without reconfigurable beam-steering at the receivers), suitably positioned to minimize crosstalk.

In this paper, we propose the design and the numerical investigation of reconfigurable Optical Wireless Interconnections Blocks (OWIBs) exploiting the beam steering capabilities of Optical Phased Arrays (OPAs), i.e. optical antenna arrays with configurable phase shifts, both at the transmitter and at the receiver sections. The feasibility of this approach is supported by the integrated large-scale phased arrays, which have been already considered for off-plane beam steering in LIDAR applications [28]. Here, we exploit the in-plane radiation of simple taper antennas to implement 1×N and N × N switching matrices. We define the design criteria and we investigate the feasibility of 1×N and N × N OWIBs. Moreover, we analyze the OWIB

Optics EXPRESS

behavior taking into account the on-chip multilayer structure, which strongly influences the wave propagation.

2. Optical wireless interconnection block

A conceptual scheme of a N × N OWIB is shown in Fig. 1, where N transmitters and N receivers are interconnected through reconfigurable antenna arrays lying on a dedicated optical layer. Figure 1 outlines a possible implementation of beam reconfigurability by OPAs made of integrated nanoantennas. In the scheme, the antennas are integrated with standard waveguides and they radiate a wavelength-division multiplexed (WDM) signal with parallel transmission of different data channels, i.e. the M different wavelengths λ. By shifting the phase of the input signals of the OPAs, through Optical Phase Shifters (OPSs), the radiated beam can be steered to communicate with a specific receiver. The phase shift necessary for the OWIB operation can be achieved in Si waveguides by using Optical Phase Shifters (OPS) based either on thermo-optic or plasma-optic effect [20].

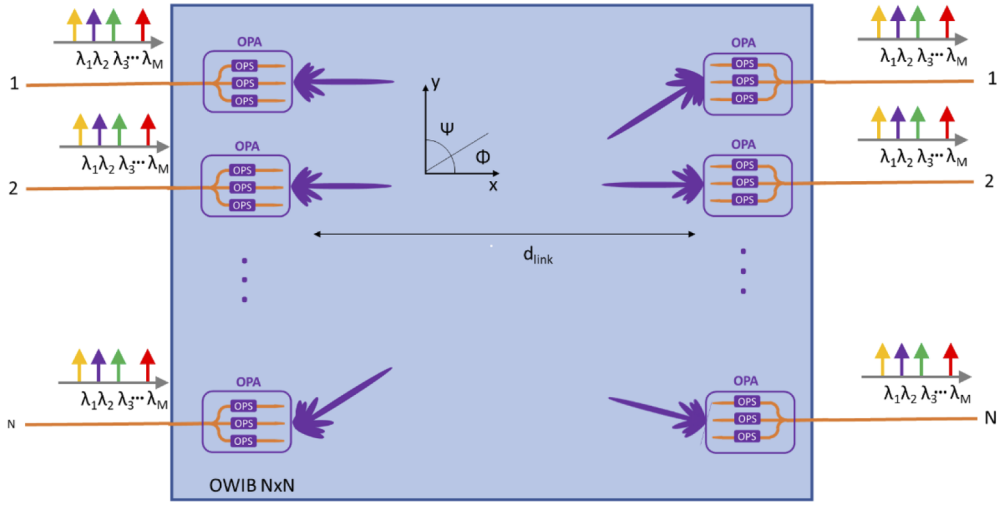

Fig. 1. Block diagram of an NxN OWIB. OPA: Optical Phase Array; OPS: Optical Phase-Shifter

The transmitting and receiving OPAs schematized in Fig. 1 are made by aligning, along the y-axis, a number of radiators. If the optical signal at each antenna in the arrays is suitably phase-shifted, e.g. by thermo-optic or plasma-optic effect, the radiation beam can be steered in the propagation plane, i.e. the xy-plane. Since the focus of this work is the analysis of the feasibility of reconfigurable on-chip optical interconnections, we will consider only very simple radiators made of inversely tapered Silicon On Insulator (SOI) waveguides. Nonetheless, the design principles proposed are virtually applicable to any kind of antenna.

2.1. Taper antenna radiation characteristics

The taper antenna in Fig. 2(a) is obtained by inversely tapering a standard SOI waveguide, with cross-section height h=220 nm and width w=450 nm. The taper is terminated on a small tip with length l=1 μm, and width w_T=130 nm. The guided mode becomes evanescent while propagating in the inverse taper and, therefore, it is radiated in the surrounding dielectric. The gradual variation of the effective refractive index in the taper guarantees a good impedance matching with the surrounding medium and a low input back-reflection (i.e. less than −35 dB). All those characteristics concur for an efficient conversion of the guided signal into wireless radiation.

Optics EXPRESS

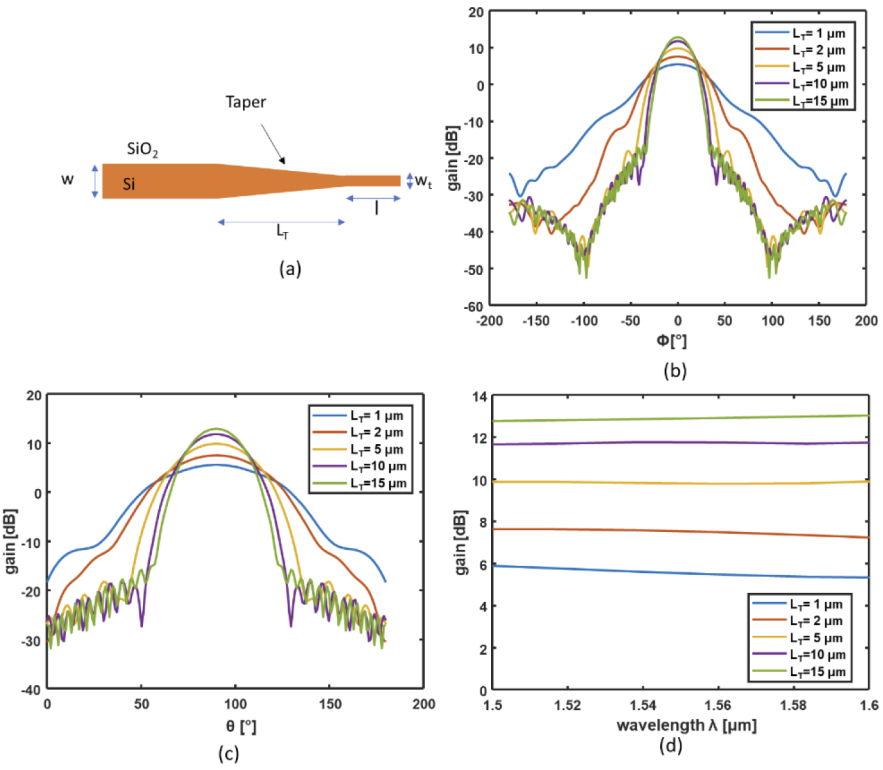

Fig. 2. (a) Scheme of the taper antenna, (b) and (c) taper antenna gain, calculated by three-dimensional FDTD simulations, as a function of the angles Φ (with θ=90° - horizontal plane) and θ (with Φ=0° - vertical plane), respectively, for different values of the taper length L_T. (d) Maximum gain of the taper antenna as a function of the wavelength for different values of the taper length L_T.

In order to evaluate its radiation characteristics, the taper antenna was modelled through the three-dimensional Finite Difference Time Domain Method (FDTD) [29]. Standard near-to-far field projections of the fields recorded on a closed box, surrounding the antenna and the SOI waveguide, were calculated after the Fourier transformation of the time-domain electromagnetic field [29]. For the analysis of the radiation characteristics of the single antenna and for the design of the OPAs, the radiators were considered as embedded into a homogenous medium with refractive index n_{SiO2}=1.445 at the wavelength λ=1.55 μm, as required for an easier computation of the near-to-far-field transformation.

Figure 2(b) and (c) show the horizontal and vertical radiation diagrams, expressed in terms of the antenna gain, as a function of the angle Φ (with θ=π/2 for the horizontal pattern) and as a function of θ (with Φ=0 for the vertical pattern), respectively, for different values of the taper length L_T. The antenna gain G(θ, Φ) is defined as:

$$G(\theta, \Phi) = 4\pi \frac{I(\theta, \Phi)}{P_{in}} \tag{1}$$

where I(θ,Φ) is the radiation intensity and P_{in} is the input power launched into the strip waveguide. The angles θ and Φ are defined according to the spherical coordinate reference system (with Φ in the xy plane shown in Fig. 1).

From Fig. 2(b) and (c), we can infer that an increase of the taper length L_T gives an increase of the antenna directivity and a narrowing of the radiated beam, even if for values of the taper length

Optics EXPRESS

above 10 μm the improvement is not significant. For this antenna, the maximum radiation occurs in the xy-plane in the direction of the wave propagation (i.e. x-direction or Φ=0 and θ=90° in spherical coordinates).

Moreover, since the taper antenna is a non-resonant structure, its radiation characteristics are almost constant with the wavelength. For example, Fig. 2(d) shows the maximum gain of the taper antenna as a function of the wavelength for different values of the taper length L_T. For all the L_T values, the variation of the maximum gain in the wavelength range from λ = 1.50 μm to λ = 1.60 μm is less than 0.7 dB.

2.2. Design criteria for the OPAs and for 1×N interconnection element

According to antenna theory [30], the overall radiation diagram of an array made of an alignment of N_a identical antennas, can be calculated by multiplying the electromagnetic field radiated by the single antenna by the so-called array factor (AF). The array factor AF is obtained by superimposing the contributions of point sources placed at the same position of each single antenna composing the array, and can be written as:

$$AF = \sum_{q=1}^{N_a} a_q e^{-j\,(q-1)\,[kd\,cos(\Psi)+\alpha]} \tag{2}$$

where a_q is the excitation amplitude of each element, $k = 2\pi n_m/\lambda$ is the propagation constant in a homogeneous medium with refractive index n_m at the wavelength λ, d is the distance between the antennas, and α is the phase shift of the input signal between two adjacent radiators. In Eq. (2), Ψ is the angle between the direction of the observation point and the axis of the linear array.

To simplify, in the following we will consider arrays with the same excitation amplitude for all the elements (uniform amplitude arrays). As a consequence, we can write $a_q = 1$. Moreover, as we are interested in interconnecting OPA on the xy plane (see Fig. 1), the AF will be expressed as a function of the angle $\Phi = \pi/2 - \Psi$, which indicates the direction of the observation point on this plane with respect to the perpendicular to the array axis. Equation (2) can therefore be rewritten in the form:

$$AF = \sum_{q=1}^{N_a} e^{-j\,(q-1)\,[kd\,sin(\Phi)+\alpha]}. \tag{3}$$

Once the overall electromagnetic field is calculated, the gain of the array can be obtained by applying Eq. (1).

In principle, different approaches for the OPA design based on the choice of the distance d between the antennas in the array are possible. From [30,31], given a fixed operating wavelength, the distance d between the antennas defines the extension of the so-called "visible region". The "visible region" ranges from $-kd$ to $+kd$ and identifies the range of variability of the exponential term $kd\,sin(\Phi)$ in Eq. (3). The phase α can be used to translate the visible range and suitably change the radiation pattern. In fact, through the choice of this parameter it is possible to tailor the radiation diagram of the array, i.e. to control the direction of the main lobe and of the nulls, the existence of grating lobes, etc.

For example, considering a broadside uniform linear array (i.e. an array with phase-shift $\alpha=0$, $a_q = 1$ and constant distance d between adjacent antennas), when $d<\frac{\lambda}{n_m}$ only one main lobe of the AF exists in the visible region. Conversely, when $d \geq \frac{\lambda}{n_m}$, multiple main radiation lobes (i.e. grating lobes) can fall in the "visible region". As we will detail in the following, this occurrence can be exploited to increase the number of connected receivers. Steering of the main lobe in the xy-plane, and therefore realization of the 1 × N interconnection, is obtained by varying the phase shift α among the excitations of the different elements.

We consider first the case of three taper antennas (N_a=3) aligned along the y direction with distance $d = \frac{3\lambda}{4n_{SiO2}}$ which allows, for a broadside array, to obtain a single main lobe in the radiation pattern. In this case, the first nulls around the main lobe are along the directions corresponding

Optics EXPRESS

to:

$$\Phi_{null} = \pm \sin^{-1}\left[\frac{\lambda}{2\pi d n_m}\left(\frac{2\pi}{N_a}\right)\right]. \quad (4)$$

Figure 3(a) shows the gain of the array as a function of the angle Φ for an array of N_a=3 taper antennas with L_T=2 μm. In particular, Fig. 5(a) illustrates the gain for three different values of the phase shift, i.e. α=0 (red curve) and α=±120° (yellow and blue curve, respectively), which are the phase shifts required to steer the maximum of the radiation diagram (i.e. α=±360°/N_a) on the same positions of the nulls of the broadside (α=0°) array. The radiation diagram of the single taper antenna is also reported (violet curve) for comparison.

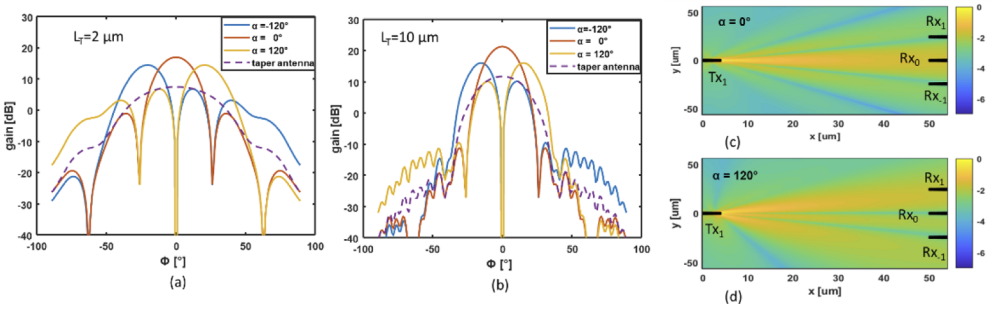

Fig. 3. Gain as a function of the angle Φ for an array of N_a=3 taper antennas with antenna distance $d = \frac{3\lambda}{4n_{SiO2}}$, and taper length (a) L_T=2 μm, and (b) L_T=10 μm, for three different values of the phase shift α=0 (red curve), and α=±120° (yellow and blue curve, respectively). The gain of the single taper antenna is also reported (violet dashed curve). Electric field pattern in the xy-plane calculated by 3D-FDTD simulations for (c) α=0, and (d) α=120°, with L_T=2 μm, d_{link}=45 μm and $\lambda = 1550\,nm$. The color bar represents the normalized amplitude of the electric field in logarithmic scale.

As this figure shows, by changing the phase α=±120° the main radiation lobe is steered of an angle Φ_{null}=±26°, which corresponds to a null of the radiation diagram when α=0° (broadside array). The radiation diagram of the single taper antenna, with its own beamwidth and its maximum for Φ=0, is responsible of the attenuation of the maximum gain of the steered beams with respect to the value of the broadside array (of about 2.5 dB). For this reason, using extremely narrow-beam radiators is not the best solution for this application.

For the sake of comparison, Fig. 3(b) shows the overall gain as a function of the angle Φ for an array of N_a=3 taper antennas with L_T=10 μm, for the same phase shift α values of Fig. 3(a). In the same figure, the gain calculated for the single taper antenna with L_T=10 μm is also reported (violet dashed curve). The behavior is similar to the one shown in Fig. 3(a), and the nulls of the radiation diagram for α=0 (red curve) occur always at Φ_{null}=±26°. As expected, by comparing Figs. 3(a) and (b), we can observe that higher gain is achieved (increase of about 4 dB) for more directive single antennas. As a counterpart, the reduction of the maximum gain of the steered beam tends to rise (≅ 5 dB), as expected for the increased gain and reduced beamwidth of the single element for Φ=0°.

It is worth mentioning that the curves reported in Fig. 3 were verified by 3D-FDTD simulation of the whole array immersed in a homogeneous medium, achieving an almost perfect agreement of the results. This confirms that, for a first design of the OWIB, it is possible to simply rely on the analytic formulation instead of simulating the complete structure.

Considering the radiation diagrams shown in Figs. 3(a) or (b), three different receivers can therefore be addressed by changing the phase of the input signal (i.e. α=0, and α=±120°), thus obtaining a 1×3 wireless switch. It is worth pointing out that the crosstalk between the different receivers can be minimized by placing them at Φ=0 and Φ=±Φ_{null} of the transmitting antenna.

Optics EXPRESS

As an example, Figs. 3(c) and (d) show the electric field pattern in the xy-plane calculated by 3D-FDTD simulation for (c) α=0°, and (d) α=120°, with a distance between the transmitter (Tx_1) and the receivers (Rx_0, and $Rx_{\pm1}$) equal to d_{link}=45 μm. The considered wavelength is $\lambda = 1550\,nm$. The color bar represents the normalized amplitude of the electric field in logarithmic scale. The geometrical position of the receiving OPAs (i.e. $Rx_{\pm1}$) was determined by the equation $y_{\pm1} = \pm d_{link}\tan(\Phi_{null})$.

Figure 3(c) qualitatively shows that, when α=0°, Rx_0 is illuminated by the main lobe, whereas both $Rx_{\pm1}$ fall in radiation minima. Similarly, as shown in Fig. 3(d), when α=120° the receiver Rx_{+1} is illuminated by the steered main lobe, whereas the other two receivers fall in radiation minima.

This configuration can therefore be used to realize a 1×3 interconnection between a transmitter and three receivers suitably positioned as previously discussed. It is now important to analyze quantitatively the performance of this device in terms of power transfer and crosstalk.

It is worth pointing out that, in order to guarantee the 1×3 interconnection, it is also necessary to virtually steer the beam of the receiving OPAs in the direction of the maximum radiation. This is feasible by properly phase-shifting the mode amplitudes of the fundamental TE mode in each waveguide at the receiving OPAs. The mode amplitude, obtained through a mode expansion monitor [29], represents the fraction of the received signal coupled into each waveguide by the corresponding antenna.

Figure 4 shows the transmittance in dB at the receiving OPAs, i.e. Rx_0, and $Rx_{\pm1}$, calculated by 3D-FDTD simulations. Each OPA, either transmitting or receiving, is made of three taper antennas with taper length L_T=2 μm, and antenna distance $d = \frac{3\lambda}{4n_{SiO2}}$. The phase shifts of the OPAs are chosen to guarantee a 1×3 interconnection between the transmitter and the receivers. Specifically, to connect the transmitter with the in-line receiver (Tx→Rx_0), with the receiver at Φ=26° (Tx→Rx_1), and with the receiver at Φ=−26° (Tx→Rx_{-1}), the phase shifts at the transmitting and at the receiving OPAs are, respectively: (a) α=0°, $\alpha_{Rx0} = \alpha_{Rx+1} = \alpha_{Rx-1} = 0°$; (b) α=120°, α_{Rx+1}=−120°, and α_{Rx0}=α_{Rx-1}=0°; (c) α=−120°, α_{Rx-1}=+120°, and α_{Rx0}=α_{Rx+1}=0°. The simulations were performed considering the propagation in a homogeneous medium with refractive index n_{SiO2}=1.445 and a link distance between TX and Rx_0 d_{link} = 45 μm. In each plot of Fig. 4, the transmittance of every link, computed as the total power coupled into the receiver waveguides divided by that at the transmitter, is reported. Transmittances are in dB scale and refer to different values of the phase shifts α at the transmitter and at the receivers. Figure 4(a) is for the case in which all the arrays are in the broadside configuration. As expected, the central receiver is the one which is better illuminated by the transmitting antenna. The transmittance of Rx_0 is, in fact, maximized. The difference between the transmittance at Rx_0 and at Rx_{+1}, or Rx_{-1}, represents the crosstalk, being these two receivers not interested in communicating with the transmitter in the considered layout.

Figure 4(b) and (c) illustrate the different scenarios in which the transmitter aims at communicating with Rx_{+1} and Rx_{-1}, respectively. In these two configurations, the link power budget between the Tx and the receiver involved in the communication is reduced with respect to the first scenario and the crosstalk is, on the contrary, increased. The reduced performance can be explained by considering the radiation diagrams of the arrays reported in Fig. 3(a) and the reciprocal path lengths between each transmitting and receiving OPAs. When communication takes place in tilted directions, in fact, the performance of the arrays is reduced, lateral lobes create more interference, and the link distance grows.

Considering Fig. 4, the worst-case crosstalk occurs between Rx_0 and either Rx_{+1} or Rx_{-1}, and it is equal to −22 dB. The insertion losses (i.e. about 20 dB for α=0°, and 24 dB for α=120°), which are due to the propagation in a homogeneous medium, agree with the well-known Friis transmission equation [31].

Optics EXPRESS

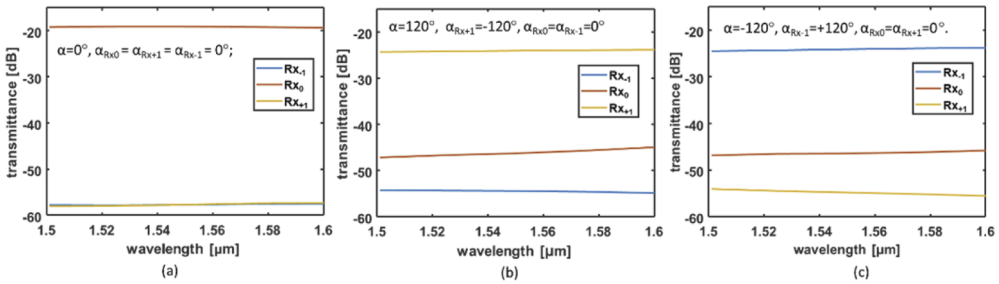

Fig. 4. Transmittance in dB, calculated by 3D-FDTD simulations, at the receiving OPAs, i.e. Rx_0 (Φ=0°), and $Rx_{\pm1}$(Φ=±26°), with three taper antennas for each array, and taper length L_T=2 μm, antenna distance $d = \frac{3\lambda}{4n_{SiO2}}$, and link distance d_{link} = 45 μm. The phase shift at the transmitting and at the receiving OPAs are, respectively: (a) α=0°, $\alpha_{Rx0} = \alpha_{Rx+1} = \alpha_{Rx-1} = 0°$; (b) α=120°, α_{Rx+1}=−120°, and α_{Rx0}=α_{Rx-1}=0°; (c) α=−120°, α_{Rx-1}=+120°, and α_{Rx0}=α_{Rx+1}=0°. The simulations were performed considering the propagation in a homogeneous medium with refractive index n_{SiO2}=1.445.

The choice of using three elements in the OPA was made in the hypothesis of simplifying the fabrication of the OWIBs and of reducing the complexity of the circuitry driving the thermal phase-shifters in a fabricated sample. Nonetheless, it is possible to realize arrays with more than three elements which are expected, from antenna theory, to have higher gain.

As an example, Fig. 5(a) shows the gain as a function of the angle Φ for an array of N_a=5 taper antennas with antenna distance $d = \frac{3\lambda}{4n_{SiO2}}$, and taper length L_T=2 μm. In particular, Fig. 3(a) illustrates the gain for three different values of the phase shift, i.e. α=0 (red curve) and α=±72° (yellow and blue curve, respectively). Also in this case, the phase shifts α=±360°/N_a steer the maximum of the radiation diagram on the same positions of the nulls of the broadside (α=0°) array. The radiation diagram of the single taper antenna is also reported (violet curve) for comparison.

Figure 5(b), (c), and (d) show the transmittance in dB at the receiving OPAs, i.e. Rx_0, and $Rx_{\pm1}$, calculated by 3D-FDTD simulations in the case of OPAs with N_a=5 taper antennas, taper length L_T=2 μm, and antenna distance $d = \frac{3\lambda}{4n_{SiO2}}$. The phase shifts at the transmitting and at the receiving OPAs are, respectively: (b) α=0°, $\alpha_{Rx0} = \alpha_{Rx+1} = \alpha_{Rx-1} = 0°$; (c) α=72°, α_{Rx+1}=−72°, and α_{Rx0}=α_{Rx-1}=0°; (d) α=−72°, α_{Rx-1}=+72°, and α_{Rx0}=α_{Rx+1}=0°. The simulations were performed considering the propagation in a homogeneous medium with refractive index n_{SiO2}=1.445 and a link distance between TX and Rx_0 d_{link} = 45 μm.

Considering Figs. 5(b), (c), and (d), the worst-case crosstalk occurs between Rx_0 and either Rx_{+1} or Rx_{-1}, and it is equal to −27 dB. The insertion losses are about 12 dB for α=0°, and 14 dB for α=72°.

Compared to the case of N_a=3 shown in Figs. 4, the insertion loss is improved of 8 dB for α=0°, and of about 10 dB for α=72°. An improvement of 5 dB of the crosstalk is also achieved. As a counterpart, since more antennas are considered, more power is expected to be required to drive the phase shifters of each OPA. In fact, if P_α is the power required for achieving a phase shift equal to α, the total power required for steering an OPA with N_a antennas can be roughly estimated as P_{OPA}=(N_a−1) P_α.

As expected from antenna theory, increasing the distance d among the radiators, leads to having multiple main lobes of the AF in the visible space. For a broadside array, this is observed when $d \geq \frac{\lambda}{n_m}$. However, as shown below, this feature can be exploited to address more receivers.

As an example, here we consider the case of OPAs made of three taper antennas (N_a=3, with taper length L_T=2 μm) aligned along the y direction as before, but with distance $d = 2\frac{\lambda}{n_{SiO2}}$. Figure 6(a) shows the corresponding overall gain of the array as a function of the angle Φ. Also in

Optics EXPRESS

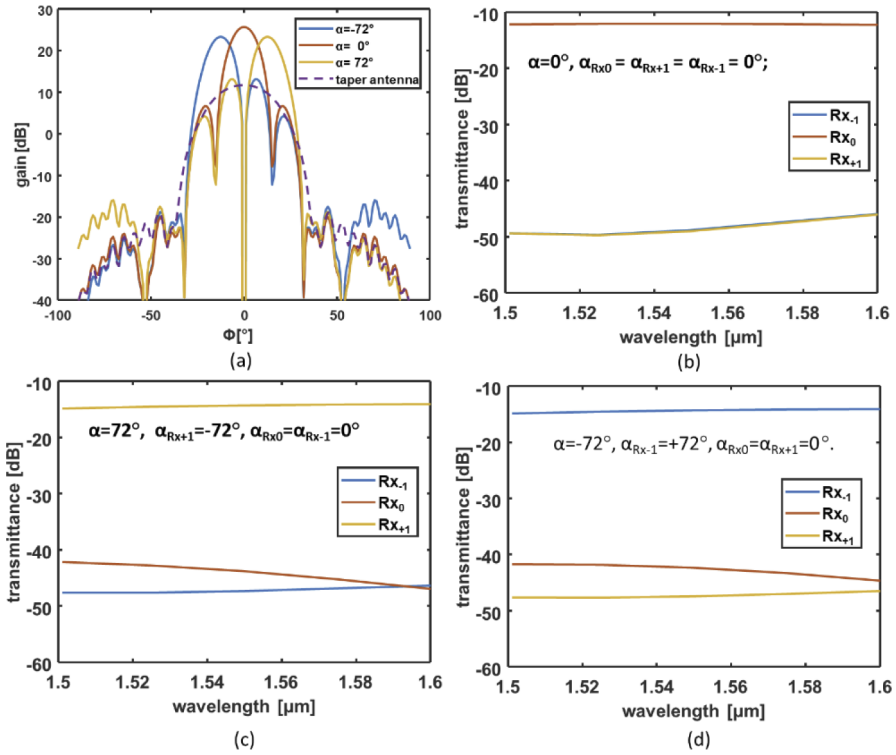

Fig. 5. (a) Gain as a function of the angle Φ for an array of N_a=5 taper antennas with antenna distance $d = \frac{3\lambda}{4n_{SiO2}}$, and taper length L_T=2 μm. (b), (c) and (d) Transmittance in dB, calculated by 3D-FDTD simulations, at the receiving OPAs, i.e. Rx_0 (Φ=0°), and $Rx_{\pm1}$(Φ=±15°), with five taper antennas for each array, and taper length L_T=2 μm, antenna distance $d = \frac{3\lambda}{4n_{SiO2}}$, and link distance d_{link} = 45 μm. The phase shift at the transmitting and at the receiving OPAs are, respectively: (b) α=0°, $\alpha_{Rx0} = \alpha_{Rx+1} = \alpha_{Rx-1} = 0°$; (c) α=72°, α_{Rx+1}=−72°, and α_{Rx0}=α_{Rx-1}=0°; (d) α=−72°, α_{Rx-1}=+72°, and α_{Rx0}=α_{Rx+1}=0°. The simulations were performed considering the propagation in a homogeneous medium with refractive index n_{SiO2}=1.445.

this case, the OPA gain was calculated from Eq. (1) applied to the 3D-FDTD simulated far-field of the taper antenna multiplied by the *AF* of Eq. (3).

As one can observe, by applying the phase shifts α=±120° (yellow and blue curve, respectively) to the array elements of the transmitter, it is possible to steer the maxima of the radiation diagrams to the new positions of the radiation nulls of the broadside array (α=0, red curve), which are now at Φ_{null}=±10°, in agreement with Eq. (4) when *d* is incremented.

With this approach it is possible to obtain a 1×5 wireless switch. In fact, by considering the radiation diagrams shown in Figs. 6(a) one can note that five different receivers can be addressed with the main radiation lobes by the transmitter through suitable phase modification of the input signals (i.e. α=0, and α=±120°). The five receivers Rx_i (with i=0, ±1, ±2) should be placed in correspondence of the radiation peaks/nulls as indicated in Fig. 6(a), according to the strategy previously adopted. Then, each receiver will select the incoming signal by using the same phase-tuning approach described for the transmitter. Also in this case, the geometrical position of the receiving OPAs (i.e. Rx_i) can be determined by the equation:

$$y_i = d_{link} \tan(\Phi_{null\_i}),$$

Optics EXPRESS

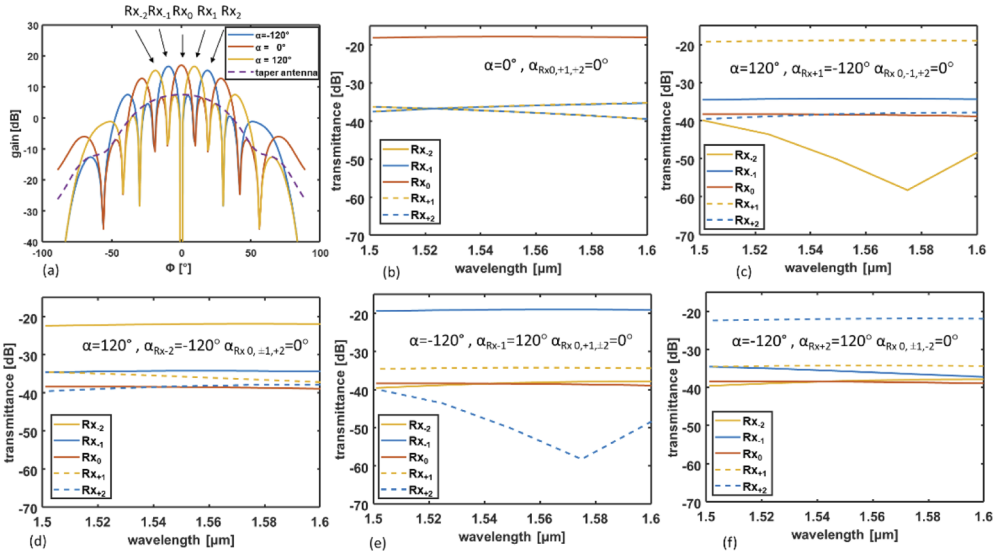

Fig. 6. (a) Gain as a function of the angle Φ for an array of N_a=3 taper antennas with antenna distance $d = 2\frac{\lambda}{n_{SiO2}}$, and taper length L_T=2 μm for three different values of the phase shift α=0 (red curve), and α=±120° (yellow and blue curve, respectively) . The gain of the single taper antenna is also reported (violet dashed curve). (b-f) Transmittance in dB, calculated by 3D-FDTD simulations, at the receiving OPAs, i.e. Rx_0, and $Rx_{\pm1}$, and $Rx_{\pm2}$ with link distance d_{link} = 45 μm. The phase shift at the transmitting and at the receiving OPAs are, respectively: (b) α=0°, $\alpha_{Rx0,\pm1,\pm2}$=0°; (c) α=120°, α_{Rx+1}=−120° $\alpha_{Rx\,0,-1,\pm2}$=0°, (d) α=120°, α_{Rx-2}=−120° $\alpha_{Rx\,0,\,\pm1,+2}$=0°, (e) α=−120°, α_{Rx-1}=120° $\alpha_{Rx\,0,+1,\pm2}$=0°, (f) α=−120°, α_{Rx+2}=120° $\alpha_{Rx\,0,\,\pm1,-2}$=0°. The simulations were performed considering the propagation in a homogeneous medium with refractive index n_{SiO2}=1.445.

with i=±1, ±2.

Figure 6(b)-(f) show the corresponding transmittances, calculated by 3D-FDTD simulation, at the receiving OPAs i.e. Rx_0, and $Rx_{\pm1}$, and $Rx_{\pm2}$ with link distance d_{link} = 45 μm. The input and output phase-shifts, necessary for the 1×5 interconnection, are reported. Also in this case, the simulations were performed considering the propagation in a homogeneous medium with refractive index n_{SiO2}=1.445.

The worst-case insertion loss, i.e. 21.87 dB, occurs when the more external receivers $Rx_{\pm2}$ are used, whereas the best performance in terms of insertion loss, i.e. 17.77 dB, pertains to Rx_0. This occurrence agrees with the radiation diagram in Fig. 6(a) where the gain peaks decrease for higher values of |Φ|. The worst-case crosstalk, i.e. −12.5 dB, occurs either between Rx_{+1} and Rx_{+2}, or between Rx_{-1} and Rx_{-2}.

Comparing the results of the reported designs of OPAs, we can state that antenna distance values $d \geq \frac{\lambda}{n_m}$ allow to increase the number of reachable receivers and give better performances in terms of insertion loss. As a further advantage, larger values of the distance d between adjacent antennas allow to prevent undesired coupling between the input waveguides. As a counterpart, the crosstalk is increased.

2.3. 3×3 optical wireless interconnection blocks

Starting from the OPA design with a distance $d = 2\frac{\lambda}{n_{SiO2}}$ among the array elements, a 3×3 matrix connecting three transmitters (I_0, and $I_{\pm1}$) and three receivers (O_0, and $O_{\pm1}$) according to the scheme shown in Fig. 7(a) can be implemented. Since the OPAs in the 3×3 matrix are

Optics EXPRESS

characterized by the radiation diagrams shown in Fig. 6(a), the communication between the further nodes (i.e. between I_{-1} and O_{+1}, and between I_{+1} and O_{-1}) is allowed by the radiation lobes denoted by $Rx_{\pm 2}$ in Fig. 6(a). The arrows in Fig. 7(a) denote the possible interconnections between the nodes and the arrow colors and line-styles follow that of the curves in Figs. 7(b)-(d).

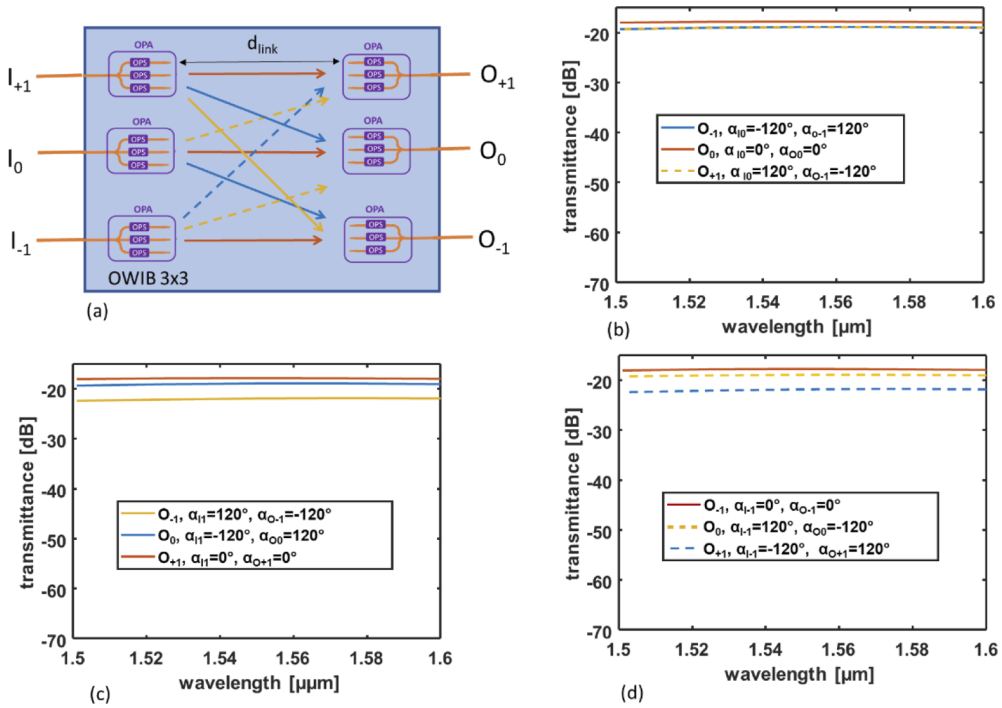

Fig. 7. (a) Scheme of the 3×3 Optical Wireless Interconnection Block, (b-d) Transmittance in dB, calculated by 3D-FDTD simulation, at the connected receiving OPAs i.e. O_0, and $O_{\pm 1}$, with three taper antennas for each array, and taper length L_T=2 μm, antenna distance $d = \frac{2\lambda}{n_{SiO2}}$, and link distance d_{link} = 45 μm. The input signal is launched at (b) I_0, (c) I_{+1}, and (d) I_{-1}. The simulations are performed considering the propagation in a homogeneous medium with refractive index n_{SiO2}=1.445.

Figure 7(b)-(d) shows the transmittance, calculated by 3D-FDTD simulation, at the receiving OPAs, i.e. O_0, and $O_{\pm 1}$, with link distance d_{link} = 45 μm. All the OPAs are made of three taper antennas, with taper length L_T=2 μm. In particular, the calculated transmittance in Figs. 7(b)-(d) pertain to the three connected receivers (i.e. O_0, and $O_{\pm 1}$), when the input signal is launched at (b) I_0, (c) I_1, and (d) I_{-1}, respectively. The input and output phase-shifts, necessary for the 3×3 interconnection block, are also reported in Figs. 7(b)-(d) and summarized in Table 1. For each input/output connection, the phase-shifts are considered equal to zero when not indicated.

Table 1. Interconnection matrix reporting the phase shifts of the transmitting and receiving OPAs needed to link the input and output ports of a 3×3 OWIB. For each input/output connection, the phase-shifts are equal to zero when not indicated.

	OUTPUT		
INPUT	O_{-1}	O_0	O_{+1}
I_{-1}	α_{I-1}=0°, α_{O-1}=0°	α_{I-1}=120°, α_{O0}=−120°	α_{I-1}=−120°, α_{O+1}=120°
I_0	α_{I0}=−120°, α_{O-1}=120	α_{I0}=0°, α_{O0}=0°	α_{I0}=120°, α_{O-1}=−120°
$I+_1$	α_{I+1}=120°, α_{O-1}=−120°	α_{I+1}=−120°, α_{O0}=120°	α_{I+1}=0°, α_{O+1}=0°

Optics EXPRESS

The behavior of the 3×3 matrix indeed follows that of the 1×5 interconnection previously described. Therefore, also in this case, the maximum calculated crosstalk is equal to −12.5 dB.

3. Effect of multipath propagation

All the results discussed above refer to 3D-FDTD simulations of the antenna arrays immersed in a homogeneous SiO_2 medium. This analysis is helpful to define the design criteria, but it neglects multipath propagation phenomena generated by the medium discontinuities existing in SOI-based on-chip optical wireless scenario. As numerically and experimentally investigated by the authors in [23], the propagation in an on-chip multilayered structure causes multiple reflections of the optical signal at the interfaces. This phenomenon can induce either an increase of the received power, thanks to constructive interference, or a fading of the signal due to destructive interference. In [23] optical wireless point-to-point links are analyzed either numerically or experimentally. The wireless links exploit the same taper antennas used in this work as transmitters and receivers. The simulation results in [23] are obtained by 3D FDTD considering the propagation in the on-chip multilayer structure, which corresponds to the fabricated sample. In [23] the numerical results are compared with the experimental ones showing a good agreement and confirming, at the same time, the presence of multi path propagation and the capability of predicting on-chip propagation by numerical simulations.

In order to verify the feasibility of the 1×5 and of the 3×3 switches in a more realistic on-chip propagation model, taking into account the multipath phenomenon, we simulated the OWIBs considering the multilayer structure in Fig. 8(a), which corresponds to the sample fabricated and already characterized in [23] for the evaluation of point-to-point wireless links. In particular, it consists of a standard SOI sample with a bottom layer of Si of thickness $h_B = 675\ \mu m$, an overlying layer of SiO_2 of $h_S = 3\ \mu m$ height, and a further layer of Silicon of $h = 220\ nm$ thickness, housing the standard Si waveguides and the taper antennas. The antenna layer is covered with a thin layer ($h_A = 300\ nm$) of borophosphorous tetraethyl orthosilicate (BPTEOS), which has a refractive index very close to the one of SiO_2 (n_{BPTEOS}=1.453). A polymer-based top layer made of UV26 of thickness $h_T = 3.78\ \mu m$ and refractive index $n_{UAV26} = 1.526$ is also considered above the BPTEOS. The SiO_2, BPTEOS, and UV26 define an overall quasi-homogenous medium, thanks to the small difference of the refractive index. The topmost layer is air, which is considered as infinite in the simulations by using Perfectly Matched Layer (PML) boundary conditions. The PML conditions were also applied to the bottom Si layer to approximate its finite thickness ($h_B = 675\ \mu m$) as infinite, and on all the lateral boundaries of the computational domain.

To better describe the effect of multipath propagation, Figs. 8(b) and (c) show the electric field pattern calculated by 3D-FDTD simulation (b) in the xz-plane for y=0 μm, and (c) in the xy-plane for z=3.61 μm, i.e. in the middle of the waveguide cross-section. The solid lines denote the geometry of the antennas and the different layers. The color bar represents the normalized amplitude of the electric field in logarithmic scale. In Fig. 8(b) and (c) a 1×5 OWIB is considered, which exploits transmitting and receiving OPAs made of three taper antennas with taper length L_T=2 μm and phase-shift α=0°. As we can see in Fig. 8(b), a sort of field-confinement effect occurs, in the vertical xz-plane, between the bottom Si- and top air-layers, where multiple reflections and transmissions occur at the interfaces. Conversely, the interfaces between SiO_2, BPTEOS, and UV26 induce negligible perturbation of the propagating electromagnetic signal. In the xy-plane (Fig. 8(c)) the field distribution basically corresponds to the radiation pattern shown in Fig. 3(a) for phase shift α=0°, with some spatial fluctuations induced by the multipath interference. The multipath effect does not seem to influence strongly the propagation, and this can relax the need for careful design of the distance between the input and the output OPAs. Nevertheless, the sensitivity of the OWIB performance to multipath interference might increase at larger distance, where reflections become more grazing and multipath propagation lengths more similar, thus supporting the reception of signal contributions with similar intensity and therefore

Optics EXPRESS

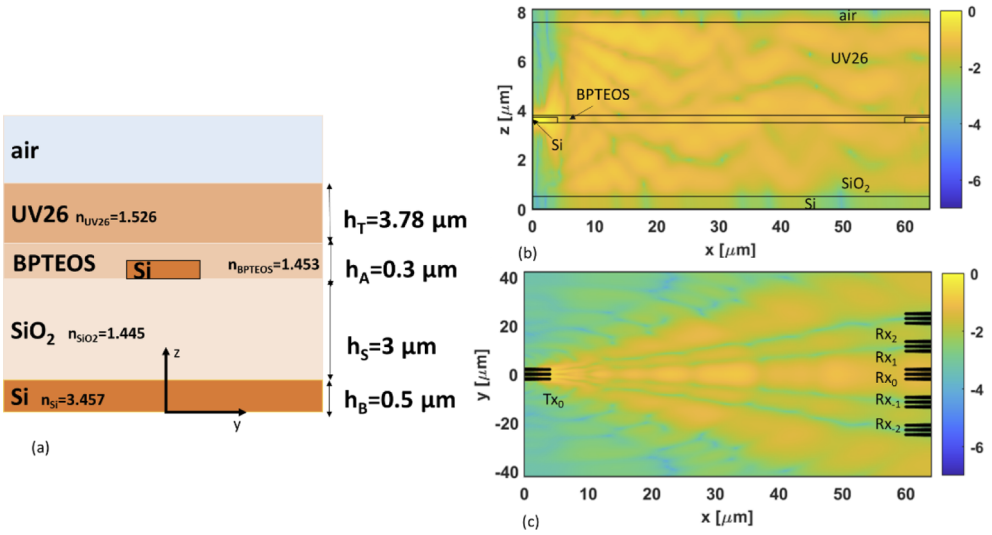

Fig. 8. (a) Scheme of the on-chip multilayered structure of the yz-cross section. A single Si waveguide is shown. (b-c) Electric field pattern calculated by 3D-FDTD simulation (b) in the xz-plane for y=0 µm, and (c) in the xy- plane for z=3.61 µm, i.e. in the middle of the waveguide cross-section, for a 1×5 OWIB with OPAs made of three taper antennas with taper length L_T=2 µm and phase-shift α=0°. The solid lines denote the geometry of the antennas and the different layers. The color bar represents the normalized amplitude of the electric field in logarithmic scale.

triggering stronger interference effects. Finally, it is also worth noting that any change in the antenna layout and/or in the layers thickness and refractive properties may affect the interference pattern – even at the shorter range – to an extent that should be investigated case by case.

As analyzed in [23], for relatively short propagation distances (i.e. up to 250 µm), the propagation in the multilayered medium can be beneficial in terms of an increase of the received power with respect to free-space propagation. However, the multipath interference phenomenon must be accounted in the OWIB design for avoiding destructive interference when choosing the position of the receivers. For this purpose, we slightly modified the initial design of the 1×5 matrix by considering an antenna distance equal to $d=2\lambda/n_{UV26}$, and by optimizing the receiving OPA position by parametric simulations.

Figure 9 shows the transmittance in dB at the receiving OPAs, i.e. Rx_0, $Rx_{\pm1}$, and $Rx_{\pm2}$, calculated by 3D-FDTD simulations for 1×5 OWIB with multilayered propagation medium. Each OPA is made of three taper antennas with taper length L_T=2 µm, and antenna distance $d = 2\frac{\lambda}{n_{UV26}}$. The phase-shifts (α, and α_{Rx}) of the OPAs are chosen to guarantee the 1×5 interconnection between the transmitter and the receivers, as indicated in Fig. 9. The reported results are obtained considering optimized values of the link distance d_{link}=55 µm and of the position of the receiving OPAs, i.e. $y_{\pm1}$=11.5 µm, and $y_{\pm2}$=23 µm, to compensate the oscillations of the received power due to the multipath effect and the perturbation of the radiation diagram induced by the multilayered medium. The behavior of the 1×5 OWIB in the multilayered medium is very similar to the one in homogeneous medium, but an increase of the maximum received power of about 8 dB is observed, due to the guiding effect of the layered structure, leading to an attenuation, as function of distance, lower than free space. The performance in terms of crosstalk is slightly worsened, since the worst-case crosstalk is equal to −11.8 dB. Similar results were achieved also for the 3×3 OWIB in the multilayered medium.

Optics EXPRESS

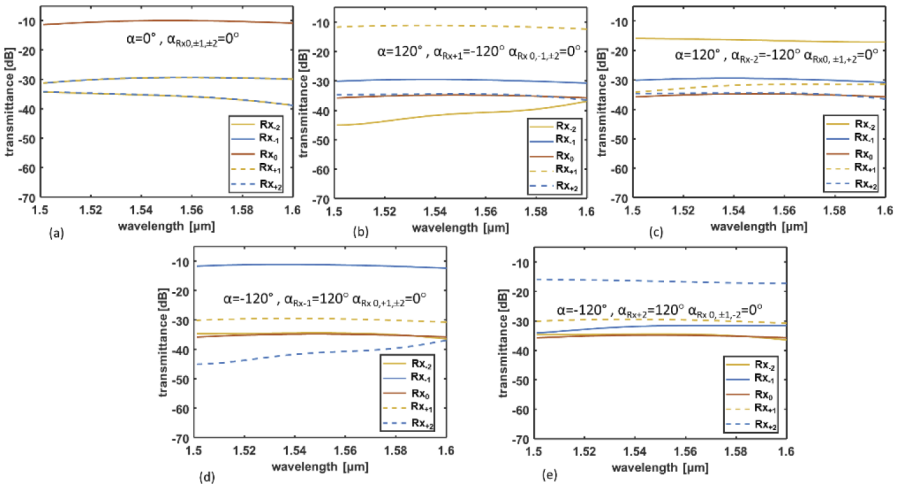

Fig. 9. Transmittance in dB as a function of the wavelength, calculated by 3D-FDTD simulation, at the receiving OPAs, i.e. Rx_0, and $Rx_{\pm1}$, and $Rx_{\pm2}$ with taper length L_T=2 μm, antenna distance $d = \frac{2\lambda}{n_{UV26}}$, and link distance d_{link} = 55 μm. The phase shift at the transmitting and at the receiving OPAs are, respectively: (a) α=0°, $\alpha_{Rx0,\pm1,\pm2}$=0°; (b) α=120°, α_{Rx+1}=−120° $\alpha_{Rx\,0,-1,\pm2}$=0°, (c) α=120°, α_{Rx-2}=−120° $\alpha_{Rx\,0,\,\pm1,+2}$=0°, (d) α=−120°, α_{Rx-1}=120° $\alpha_{Rx\,0,+1,\pm2}$=0°, (e) α=−120°, α_{Rx+2}=120° $\alpha_{Rx\,0,\,\pm1,-2}$=0°. The simulations are performed considering the propagation in the multilayered medium of Fig. 8(a).

Owing to the wireless propagation, insertion losses are not negligible. To overcome this problem, different approaches are possible. As described above, by increasing the number of antennas, the gain of the OPA can be raised (e.g. with 3 antennas the maximum gain is 21 dB, whereas for 5 antennas it is 25 dB). Moreover, the maximum gain can be also improved by increasing the directivity of the antenna elements in the OPAs by using directors or lateral gratings [32,33,22,28]. More complex optimization procedures such as particle-swarm optimization can be also applied to design the antenna geometrical parameters [34,35].

A further way of improving this device with respect to the insertion losses is related to the engineering of the wireless channel characteristics. As shown by the results, the propagation in the multilayered on-chip medium can lead to a significant reduction of the insertion losses (e.g. reduction of 8 dB in the reported examples), provided the optimized design of the OWIB and of the propagation medium (e.g. by the choice of the cladding materials and of the thickness of the layers).

It is worth pointing out that, as Fig. 9 shows, the variation of the transmittance spectra with the wavelength is very limited, thus guaranteeing broadband operation, that can largely include the complete C-band.

To maintain this broadband feature, it is very important to realize wideband phase shifters, avoiding the use of resonant structures. To this purpose, phase shifters based on thermo-optic or plasma-optic effects could be used. For example, considering the results reported in [36], a phase shift of 120° can be obtained, in a SOI waveguide, by thermo-optic effect with a 320 μm-long OPS. The estimated heater power, necessary for phase-shifting, is of about 15 mW. For the connection of one transmitter and one receiver in the OWIB, the phase-shift the OPAs would require roughly 60 mW.

The main benefit of the proposed OWIB is the large bandwidth when compared to MRR resonators. For example, if a WDM signal is used for communication, with channel spacing

Optics EXPRESS

$\Delta\lambda$=0.8 nm virtually about 120 channels can be allocated in the simulated 100-nm bandwidth of the OWIB. Given the broadband behavior of the OWIB, the power requiremed for signal routing is independent from the number of WDM channels. Therefore, it is apparent that the proposed device performances are more attractive when the number of channels scales up.

Conversely, in MRR-based networks, the power required for routing would grow with the number of channels owing to the increased number of resonators necessary for communication (e.g. about 2-mW power is needed for thermo-optic switching of a single MRR [37] and about 20 µW per MRR are required for resonance tuning [38]).

As a counterpart, propagation losses tend to be higher for wireless propagation with respect to MRR based networks [39–42]. Considering insertion losses, the OWIB concept becomes competitive when the number of MRR, required for routing a large number of WDM channels, increases (e.g. typically, insertion losses for a single MRR are 2 dB in the on-state and about 0.9 dB for a MRR in the off-state [40]).

The fabrication process necessary to realize the proposed antenna arrays involve very well-established and robust fabrication steps for a SOI platform. The taper antenna, considered as a passive non-tunable structure, can be realized through patterning of the SOI sample though deep-submicron precision Electron Beam Lithography (EBL). Such a powerful tool is particularly suitable for the realization of the nanometric scale dielectric antennas. At this stage, some issues can arise from the resist layer deposited over the waveguides. Indeed, if the taper becomes very narrow (e.g., 200 nm or less) the resist polymer, due to its low density, encounters problem in keeping firm above the taper shape, with the risk of spreading over a larger surface, thus compromising the precision in the following etching process. To circumvent this problem, a secondary, auxiliary pattern is written in the EBL process, that allows sustaining the resist layer, preventing it from spreading. After the EBL patterning, Reactive Ion Etching (RIE) is required for the realization of the antennas and the waveguide; in the same process, the auxiliary pattern is canceled. A planarized dielectric cladding can be deposited through Plasma-Enhanced Chemical Vapour Deposition (PECVD), to cover the antenna layer. Moreover, in order to realize the electrodes for thermal tuning of the antenna arrays, the deposition of high-quality metallic layers can be performed through evaporation and lift-off techniques.

For guaranteeing their correct execution, all the fabrication steps can be checked and validated through several metrology techniques, such as Ellipsometry and Scanning Electron Microscopy (SEM). However, any unlikely significant impairment on the waveguides or electrodes size due to fabrication imperfections that could impact on the OPA performance can in principle be compensated by an opportune network calibration.

4. Conclusion

In this paper, we have proposed the design of Optical Wireless Interconnection Blocks based on OPAs for on-chip communications between multiple transmitters and receivers. The design criteria of the OPAs have been identified and the performances of 1×3, 1×5, and 3×3 switching matrices have been evaluated by 3D-FDTD simulations. The effect of multipath propagation in the on-chip multilayered medium was also analyzed, showing that an improvement of the insertion loss of about 8 dB can be achieved by optimized design. Considering the proposed device to be realized in integrated silicon photonics technology, it can guarantee a broadband behavior that allows a very good scalability in terms of WDM channels, and a consequent increase of the energy per bit efficiency.

Assuming chip-scale interconnection as the main target application for the proposed device, the non-resonant nature of the proposed system, exploiting broadband antennas, can lead to a reduction of the overall amount of MRRs in the network (being the use of these components necessary only as modulators and not as switching elements), to an improvement of the overall power budget, and to the possibility of switching multiple wavelengths on a single OPA. We

Optics EXPRESS

expect the proposed optical wireless technology to substantially cut down on the number of instantiated MRRs, on the static power overhead, and on the signal-to-noise ratio over guided photonics for chip-scale connectivity, which would pave the way for a new class of densely integrated chips better equipped to tackle the daunting challenge of massive-scale data processing.

Disclosures. The authors declare no conflicts of interest.

Data availability. Data underlying the results presented in this paper are not publicly available at this time but may be obtained from the authors upon reasonable request.

References

1. B. Parhami, "Computer Architecture for Big Data," in *Encyclopedia of Big Data Technologies*, S. Sakr and A. Y. Zomaya, eds. (Springer, Cham., 2019).
2. M. Zia, C. Wan, Y. Zhang, and M. Bakir, "Electrical and photonic off-chip interconnection and system integration," in *Woodhead Publishing Series in Electronic and Optical Materials, Optical Interconnects for Data Centers*, (Woodhead Publishing, 2017).
3. J. Flich and D. Bertozzi, *Designing Network-on-Chip Architectures in the Nanoscale Era* (CRC Press, 2019).
4. G. P. Nychis, C. Fallin, T. Moscibroda, O. Mutlu, and S. Seshan, "On-chip networks from a networking perspective: Congestion and scalability in many-core interconnects," SIGCOMM Comput. Commun. Rev. **42**(4), 407–418 (2012).
5. G. De Micheli, "Keynote Talk: NoCs: A Short History of Success and a Long Future," in *Proceedings of 2018 Twelfth IEEE/ACM International Symposium on Networks-on-Chip (NOCS)*, Turin, Italy, (2018), pp. 1–2.
6. S. Werner, J. Navaridas, and M. Luján, "A Survey on Optical Network-on-Chip Architectures," ACM Comput. Surv. **50**(6), 1–37 (2018).
7. 7. N. Terzenidis, M. Moralis-Pegios, S. Pitris, G. Mourgias-Alexandris, C. Mitsolidou, K. Fotiadis, K. Vyrsokinos, T. Alexoudi, and N. Pleros, "Board- and rack-scale optical interconnection architectures for disaggregated data centers," Proc. SPIE 11286, Optical Interconnects XX, 1128606 (28 February 2020);
8. Mahdi Tala, Oliver Schrape, Milos Krstic, and Davide Bertozzi, "Interfacing 3D-stacked Electronic and Optical NoCs with Mixed CMOS-ECL Bridges: a Realistic Preliminary Assessment," In *Proceedings of the 2018 on Great Lakes Symposium on VLSI (GLSVLSI '18)*, (2018), pp. 81–86
9. Y. Thonnart, S. Bernabé, J. Charbonnier, C. Bernard, D. Coriat, C. Fuguet, P. Tissier, B. Charbonnier, S. Malhouitre, D. Saint-Patrice, M. Assous, A. Narayan, A. Coskun, D. Dutoit, and P. Vivet, "POPSTAR: A Robust Modular Optical NoC Architecture for Chiplet-based 3D Integrated Systems," *Proceedings of the 2020 Design, Automation and Test in Europe Conference and Exhibition, DATE 2020, art. no. 9116214*, (2020) pp. 1456–1461
10. A. Shacham, K. Bergman, and L. P. Carloni, "Photonic networks-on-chip for future generations of chip multiprocessors," IEEE Trans. Comput. **57**(9), 1246–1260 (2008).
11. Ruiqiang Ji, Lin Yang, Lei Zhang, Yonghui Tian, Jianfeng Ding, Hongtao Chen, Yangyang Lu, Ping Zhou, and Weiwei Zhu, "Microring-resonator-based four-port optical router for photonic networks-on-chip," Opt. Express **19**(20), 18945–18955 (2011).
12. I. Datta, D. Datta, and P. P. Pande, "BER-based power budget evaluation for optical interconnect topologies in NoCs," in *Proceedings of IEEE International Symposium on Circuits and Systems (ISCAS)*, Seoul, (2012), pp. 2429–2432
13. A. Coskun, "System-Level Optimizations for 2.5D-Integrated Chips with Silicon Photonic Links", invited talk at D43D Workshop 2018
14. S. Werner, J. Navaridas, and M. Luján. "A Survey on Optical Network-on-Chip Architectures", ACM Computing Surveys, (December 2017), Article No. 89
15. S. Deb and H. K. Mondal, "Wireless network-on-chip: a new era in multi-core chip design," in *Proceedings of 25nd IEEE International Symposium on Rapid System Prototyping*, New Delhi, (2014), pp. 59–64
16. X. Timoneda, S. Abadal, A. Franques, D. Manessis, J. Zhou, J. Torrellas, E. Alarcón, and A. Cabellos-Aparicio, "Engineer the Channel and Adapt to it: Enabling Wireless Intra-Chip Communication," IEEE Transactions on Communications **68**(5), 3247–3258 (2020).
17. S. Abadal, A. Mestres, J. Torrellas, E. Alarcon, and A. Cabellos-Aparicio, "Medium Access Control in Wireless Network-on-Chip: A Context Analysis," IEEE Commun. Mag. **56**(6), 172–178 (2018).
18. S. Foulon, S. Pruvost, D. Pache, C. Loyez, and N. Rolland, "A 142 GHz fully integrated wireless chip to chip communication system for high data rate operation," in *Proceedings of the ESSCIRC (ESSCIRC)*, Bucharest, Romania, (2013), pp. 77–80.
19. S. Abadal, S. E. Hosseininejad, A. Cabellos-Aparicio, and E. Alarcón, "Graphene-Based terahertz antennas for area-constrained applications," in *Proceedings of the 40th International Conference on Telecommunications and Signal Processing (TSP)*, Barcelona, Spain, (2017), pp. 817–820
20. W.N. Ye and Y. Xiong, "Review of silicon photonics: history and recent advances," J. Mod. Opt. **60**(16), 1299–1320 (2013).
21. L. Tsybeskov, D. J. Lockwood, and M. Ichikawa, "Silicon Photonics: CMOS Going Optical," Proc. IEEE **97**(7), 1161–1165 (2009).
22. C. García-Meca, S. Lechago, A. Brimont, A. Griol, S. Mas, L. Sánchez, L. Bellieres, N. S. Losilla, and J. Martí, "On-chip wireless silicon photonics: from reconfigurable interconnects to lab-on-chip devices," Light Sci Appl **6**(9), e17053 (2017).

Optics EXPRESS

23. J. Nanni, G. Bellanca, G. Calò, A. Badrul, E. Kaplan, M. Barbiroli, F. Fuschini, J. S. Dehkordi, V. Tralli, P. Bassi, and V. Petruzzelli, "Multi-path propagation in on-chip optical wireless links," IEEE Photonics Technol. Lett. **32**(17), 1101–1104 (2020).
24. G. Bellanca, G. Calò, A.E. Kaplan, P. Bassi, and V. Petruzzelli, "Integrated Vivaldi plasmonic antenna for wireless on-chip optical communications," Opt. Express **25**(14), 16214–16227 (2017).
25. G. Calò, G. Bellanca, B. Alam, A. E. Kaplan, P. Bassi, and V. Petruzzelli, "Array of plasmonic Vivaldi antennas coupled to silicon waveguides for wireless networks through on-chip optical technology - WiNOT," Opt. Express **26**(23), 30267–30277 (2018).
26. M. Elsaid, K. R. Mahmoud, M. F. O. Hameed, S. S. A. Obayya, and M. Hussein, "Broadband directional rhombic nanoantenna for optical wireless communications systems," J. Opt. Soc. Am. B **37**(4), 1183–1189 (2020).
27. M. Elsaid, K. R. Mahmoud, M. Hussein, M. F. O. Hameed, and S. S. A. Obayya, "Improvement of sectoral horn nanoantenna based on arc directors for point to point communications," Opt Quant Electron **53**(3), 141 (2021).
28. J. Sun, E. Timurdogan, A. Yaacobi, E. S. Hosseini, and M. R. Watts, "Large-scale nanophotonic phased array," Nature **493**(7431), 195–199 (2013).
29. Lumerical Solutions, Inc. http://www.lumerical.com/tcad-products/fdtd/
30. Robert E. Collin, *Antennas and radiowave propagation*, (McGraw-Hill, 1985).
31. J. D. Kraus, *Antennas*, (2nd Ed., McGraw-Hill, 1988).
32. G. Calò, B. Alam, G. Bellanca, F. Fuschini, M. Barbiroli, V. Tralli, and V. Petruzzelli, "Dielectric and plasmonic Vivaldi antennas for on-chip wireless communication," in *Proceedings of 2019 21st International Conference on Transparent Optical Networks (ICTON)*, (IEEE 2019), pp. 1–4.
33. H. Xu and Y. Shi, "Diffraction engineering for silicon waveguide grating antenna by harnessing bound state in the continuum," Nanophotonics **9**(6), 1439–1446 (2020).
34. L. Lobachinsky and A. Bahabad, "Using Particle Swarm Optimization to Design Broadband Optical Nano-antennas for Nonlinear Optics," in *Frontiers in Optics 2014, OSA Technical Digest (online)* (Optical Society of America, 2014), paper FTh4E.3.
35. M. F. Pantoja, A. R. Bretones, F. G. Ruiz, S. G. Garcia, and R. G. Martin, "Particle-Swarm Optimization in Antenna Design: Optimization of Log-Periodic Dipole Arrays," IEEE Antennas Propag. Mag. **49**(4), 34–47 (2007).
36. M. Jacques, A. Samani, E. El-Fiky, D. Patel, Z. Xing, and D. V. Plant, "Optimization of thermo-optic phase-shifter design and mitigation of thermal crosstalk on the SOI platform," Opt. Express **27**(8), 10456–10471 (2019).
37. N. Sherwood-Droz, H. Wang, L. Chen, B. G. Lee, A. Biberman, K. Bergman, and M. Lipson, "Optical 4×4 hitless silicon router for optical Networks-on-Chip (NoC)," Opt. Express **16**(20), 15915–15922 (2008).
38. M. Ortín-Obón, M. Tala, L. Ramini, V. Viñals-Yufera, and D. Bertozzi, "Contrasting Laser Power Requirements of Wavelength-Routed Optical NoC Topologies Subject to the Floorplanning, Placement, and Routing Constraints of a 3-D-Stacked System," IEEE Trans. VLSI Syst. **25**(7), 2081–2094 (2017).
39. D. A. B. Miller, "Attojoule Optoelectronics for Low-Energy Information Processing and Communications," J. Lightwave Technol. **35**(3), 346–396 (2017).
40. P. DasMahapatra, R. Stabile, A. Rohit, and K. A. Williams, "Optical crosspoint matrix using broadband resonant switches," IEEE J. Sel. Top. Quantum Electron. **20**(4), 1–10 (2014).
41. P. Pintus, M. Hofbauer, C. L. Manganelli, M. Fournier, S. Gundavarapu, O. Lemonnier, F. Gambini, L. Adelmini, C. Meinhart, C. Kopp, F. Testa, H. Zimmermann, and C. J. Oton, "PWM-Driven Thermally Tunable Silicon Microring Resonators: Design, Fabrication, and Characterization," Laser Photonics Rev. **13**(9), 1800275 (2019).
42. F. Testa, S. Tondini, F. Gambini, P. Velha, A. Bianchi, C. Kopp, M. Hofbauer, C. L. Manganelli, N. Zecevic, S. Faralli, G. Pares, R. Enne, A. Serrano, B. Goll, G. Fontana, A. Chalyan, J.-M. Lee, P. Pintus, G. Chiaretti, H. Zimmermann, L. Pavesi, C. J. Oton, and S. Stracca, "Integrated reconfigurable silicon photonics switch matrix in IRIS project: Technological achievements and experimental results," J. Lightwave Technol. **37**(2), 345–355 (2019).